Contents of this file

1. Equations of motion and description of numerical approach to solving them.

2. Table summarising model parameters.

3. Summary of spherical harmonic expansion used to estimate surface deflections.

4. Figures S1 to S19.

S1   Introduction

This Supporting Information document includes an extended description of the equations of motion solved to predict mantle convection. It summarises the numeric approach adopted to solve them using the TERRA code, the spherical harmonic expansion and model parameters. The approaches used to calculate surface deflections are included with the main manuscript.

This document also includes nineteen figures in three groups. First, Figures S1–S2 summarise the setup of the numerical simulations, and show examples of results and resultant surface deflections. They expand upon the results shown in Figures 1–2 in the main manuscript. Secondly, Figures S3–S7 show surface deflections and sensitivity kernels calculated by solving the equations of motion analytically using the propagator matrix approach and associated statistics. They show results for models that include self-consistent radial gravitation and removal of shallow structure, expanding upon the results shown in Figures 3–5 in the main manuscript. Figures S8–S14 show calculated vertical surface deflections from models in which viscosity and density are modified. These figures includes comparisons of surface deflections calculated using the different approaches (numeric and analytic) and model parametrizations. They extend the results shown in Figures 7–8 in the main manuscript. Figures S15–S19 show effective contributions from density anomalies in the mantle to instantaneous surface deflections. In the main text, we show spherical harmonic solutions up to a maximum spherical harmonic degree $l = 50$ (see Figure 9 in the main manuscript). Here, results are presented for maximum degrees 40, 30, 20, 10 and 5. The results demonstrate the importance of contributions from short wavelength (high degree) density structure to surface deflections, especially at shallow depths.

S2   Equations Governing Predicted Mantle Convection

In the main manuscript we explore how calculated surface deflections are impacted by the choice of methodology and assumptions used in solving equations of motion for mantle convection. This section expands on the numeric approach used to solve the equations. The analytic approach is discussed in the main manuscript.

Theoretical predictions of surface displacements from mantle convection arise from the application of physical laws that take the form of conservation equations for mass, momentum and energy (see, e.g., Hager and O'Connell, 1981; Parsons and Daly, 1983). Here, we solve those equations across a 3D spherical domain using the finite element code TERRA (Baumgardner, 1985; Bunge and Baumgardner, 1995, etc.). Under this formulation, theoretical convection in an incompressible fluid can be expressed by the following three dimensionless equations (e.g., Baumgardner, 1985; Davies et al., 2013; McKenzie et al., 1974; Parsons and Daly, 1983). First, the continuity condition for conservation of mass,

$$\nabla \cdot \mathbf{u} = 0, \tag{S1}$$

where $\mathbf{u}$ is the fluid velocity vector. Since the Prandtl number is likely to always be extremely large in this system—mantle viscosity is expected to be many orders of magnitude larger than the product of density and thermal diffusivity—inertial terms can be neglected (e.g., Parsons and Daly, 1983). Second, the equation of motion,

$$\nabla\sigma = -\rho'\mathbf{g}, \tag{S2}$$

where

$$\rho' = -\alpha\rho_0(T - T_{\text{ref}}). \tag{S3}$$

σ is the 3×3 stress tensor where the (radial) hydrostatic component balancing the reference density structure has been subtracted, ρ' is the density difference due to temperature, α is the coefficient of thermal expansion, T is temperature, T_{ref} is a radially varying reference temperature structure, which has a constant value in the mid-mantle and joins to a cold thermal boundary layer near the surface and a hot one at the CMB, reaching the surface, T_s, and core mantle boundary, T_{CMB} temperatures at the respective boundaries, and $\mathbf{g}$ is gravitational acceleration acting radially (see Table S1). This stress tensor σ_{ij} is decomposed into deviatoric and lithostatic components:

$$\sigma_{ij} = \tau_{ij} - p\delta_{ij}, \tag{S4}$$

where τ_{ij} is the deviatoric stress tensor, p is dynamic pressure and δ_{ij} is the Kronecker delta function. The deviatoric stress tensor and the strain-rate tensor, $\dot{\epsilon}_{ij}$, are related by:

$$\tau_{ij} = 2\eta\dot{\epsilon}_{ij} = \eta\left(\frac{\partial\mathbf{u}_i}{\partial x_j} + \frac{\partial\mathbf{u}_j}{\partial x_i}\right), \tag{S5}$$

where η is viscosity, and $\partial/\partial x_i$ is the spatial partial derivative. By combining equations S2, S4 and S5 we solve the equation of motion:

$$\frac{\partial(\eta\epsilon_{ij})}{\partial x_j} - \frac{\partial p}{\partial x_i} = -\rho'g\delta_{ir}, \tag{S6}$$

where g is the scalar value of $\mathbf{g}$ and δ_{ir} is the Kronecker delta selecting the radial direction r.

We first examine predictions from models in which viscosity varies only with depth, i.e., $\eta = \eta_0 \times \eta_r$, where η_0 is reference viscosity (see Table S1), and η_r is a scaling factor dependent only on radius, plotted with model results as appropriate throughout this manuscript. We then include temperature dependence of viscosity, i.e., $\eta = \eta_0 \times \eta_r \times \eta_T$, where

$$\eta_T = \exp(z' - 2T'). \tag{S7}$$

Dimensionless depth, $z' = z/d$, where $d = z_{\text{surface}} - z_{\text{CMB}} = 2890$ km, and dimensionless temperature $T' = (T - T_s)/(T_{\text{CMB}} - T_s)$, where $T_{\text{CMB}} - T_s = 2700$ K.

Finally, the heat transport equation is solved to ensure conservation of energy:

$$\frac{\partial T}{\partial t} + \mathbf{u}\cdot\nabla T = \kappa\nabla^2 T + \frac{H}{C_p}, \tag{S8}$$

where κ is thermal diffusivity, H is internal heat generation and C_p is specific heat capacity. See Table S1 for parameter values and units. Heat generation within the mantle depends on the distribution of radiogenic isotopes (e.g., Ricard, 2015).

Concentrations of such elements can be tracked in TERRA, using particles, varying as a consequence of flow and melting (see, e.g., Panton et al., 2023; van Heck et al., 2016, for full explanation). The bulk composition field, C, which varies between 0 and 1, is also tracked on particles and calculated for each of the finite elements in the model. The end-members represent completely depleted/harzburgitic material ($C = 0$), and fully enriched/basaltic material ($C = 1$). As a result, radiogenic heat production across the whole mantle volume varies, being ≈ 24 TW (5.8×10^{-12} W kg^{-1}) at 1.2 Ga, and ~ 18 TW (4.5×10^{-12} W kg^{-1}) by 0 Ma. Simulations are initialised such that the average mantle composition is $C = 0.20$ (Panton et al., 2023), and composition obeys the conservation equation:

$$\frac{\partial C}{\partial t} = -\nabla \cdot (C\mathbf{u}). \tag{S9}$$

S2.1 Numerical Modelling Strategy

The Stokes equations described above are solved by the finite element method on a series of stacked spherical shells composed of nodes based on a subdivision of a regular icosahedron, with an identical geometry for each shell when projected onto the CMB (see, e.g., Figure 1 of Baumgardner, 1985). The radial spacing of consecutive shells is 45 km, which is the same as the mean horizontal spacing of the elements across the entire model domain. The stacking of identically partitioned shells leads to a finer mean horizontal resolution of ≈ 33 km at the CMB, and a coarser resolution of ≈ 60 km at the surface. The surfaces of the uppermost elements in the shallowest shell lie at zero depth. To enable estimates of stress from these models to be directly compared with analytical solutions obtained from Green's functions across layer boundaries, the predicted values of deviatoric stress were calculated using the calculated velocities from the nearest shells using the interpolating linear shape functions of the underlying finite elements, while the dynamic pressure is calculated directly at the surface (see the main manuscript).

Each numerical model presented in this paper has two computational stages: 'spin-up', which is used to initialize the model, and the geologically more realistic 'main' stage, from which we generate predictions of surface deflections. The spin-up stage includes 2.2 billion years of model run-time. It has the following conditions imposed to avoid sharp velocity and temperature gradients, and sudden reorganization of mantle flow when the main model starts. First, a free-slip condition is imposed at the surface. Second, an initial, random white noise temperature field generated with power across spherical harmonic degrees 1-19, is inserted. Mean mantle temperature is initially 2000 K. Mantle convection arises naturally over the first two billion years of model run-time. A fixed-slip surface velocity condition is then applied to the surface for 200 Ma. These velocities are set to be equal to those at 1 Ga extracted from the reconstructions of Merdith et al. (2021); the vertical component of slip is zero. The resultant mantle structure is used as the initial condition for the main model.

The main model routine predicts flow from 1 Ga to the present-day (0 Ma). It includes an isothermal condition imposed at the surface, $T_s = 300$ K. A fixed-slip condition is imposed such that the vertical component of $\mathbf{u}$ is zero. Horizontal slip is prescribed using the plate reconstructions of Merdith et al. (2021); these are applied in 1 Ma long stages. As such, stirring by plate drift and slab sinking play a role in driving mantle flow in these models. An isothermal condition is also imposed at the core-mantle boundary such that $T_{\text{CMB}} = 3000$ K. A free-slip velocity boundary condition is imposed there, so the radial component of the mantle flow velocity ($\mathbf{u_r}$) $= 0$. While this radial velocity boundary condition is of the Dirichlet type, in a free-slip boundary condition no tangential restriction is imposed on the flow velocity but rather on the tangential deviatoric stresses acting on the boundary ($\tau_{r\theta}$, $\tau_{r\phi}$ where r, θ and ϕ are the radial and two tangential directions respectively), which are zero. Horizontal components of slip are allowed to naturally emerge and evolve subject to lowermost mantle flow. Plume behaviour is not artificially suppressed or instigated.

To ensure numerical stability and computational accuracy in these simulations, the reference viscosity, η_0, is set to 4×10^{21} Pa s. This value is probably an order of magnitude greater than the viscosity of the actual upper mantle (e.g., Forte, 2007; Ghelichkhan et al., 2021; Mitrovica and Forte, 2004, and references therein). Consequently, flow velocities in the simulations are likely to be significantly slower than in actuality. An obvious cause for concern is that using actual (comparatively fast) plate velocities as surface boundary conditions atop a relatively slowly convecting 'mantle' is likely to induce unrealistic flow.

To address this issue, imposed plate velocities are scaled such that the root-mean squared (RMS) values of the actual applied velocities (≈ 5 cm yr^{-1} unscaled) match RMS values of surface velocities (≈ 2.5 cm yr^{-1}) calculated during the spin-up phase (before plate velocities are imposed on the model) when the model mantle is convecting naturally and not being driven by surface velocities. The applied surface plate velocities are therefore scaled by a factor of 0.5 (i.e., 2.5/5) in the simulations examined in this study. To ensure that volumetric fluxes through ridges and subduction zones are realistic, simulation run times are increased by a factor of 2; i.e., the 1 Myr long plate stages are run for twice their elapsed time (2 Myr), but at half the speed. All times stated throughout the rest of this manuscript refer to times re-scaled for real-world comparison; i.e., the actual age of the respective plate stage.

For the reference case (Model 1), these conditions lead to the density distributions shown in Figure S1. Surface layer density anomalies occur only as a result of predicted compositional variation, since the surface temperature, T_s, is constant globally. This model represents the first of two reference numerical models examined in this contribution. It has the radial viscosity structure shown in Figure 2c of the main manuscript. Later, in the main manuscript, we investigate a second numerical model incorporating temperature-dependent viscosity (Equation S7). In the main manuscript we describe numeric and analytic approaches that use output from these models to calculate instantaneous surface deflections. Both approaches make use of spherical harmonics.

Table S1. Summary of Model Parameters.

Parameter	Symbol	Value	Units
Surface temperature	T_s	300	K
Core-mantle boundary temperature	T_{CMB}	3000	K
Internal heating rate	H	See text.	W kg^{-1}
Thermal expansivity	α	2.5×10^{-5}	K^{-1}
Thermal conductivity	K	4	W m^{-1}K^{-1}
Thermal diffusivity	κ	8.08×10^{-7}	m^{2}s^{-1}
Specific heat capacity	C_p	1100	J kg^{-1}K^{-1}
Reference viscosity	η_0	4×10^{21}	Pa s
Reference density	ρ_0	4500	kg m^{-3}
Overlying fluid density	ρ_w	1 or 1030	kg m^{-3}

S3   Spherical Harmonics

Any real, square-integrable function over the surface of the Earth can be described as a function of longitude θ and latitude ϕ by a linear combination of spherical harmonics of degree l and order m,

$$f(\theta,\phi) = \sum_{l=1}^{L} \sum_{m=-l}^{l} f_{lm} Y_{lm}(\theta,\phi). \tag{S10}$$

The spherical harmonic functions Y_{lm} are the natural orthogonal set of basis functions on the sphere, and f_{lm} are the spherical harmonic coefficients. As an example, Figure 2d in the main manuscript shows spherical harmonic expansion of the surface stress field predicted by Model 1 at 0 Ma (cf. Figure 2a in the main manuscript). We call this result Model 1b, and the original, full-resolution numerical result is referred to as Model 1a. The fidelity of the spherical harmonic expansion is demonstrated by the similarity of the maps and histograms shown in panels a–b and d–e of Figure 2 in the main manuscript.

$$P_l = \sum_{m=-l}^{l} f_{lm}^2 \tag{S11}$$

140   gives the total power across all spherical harmonics of a given degree l. Average power for each mode m within degree l, $\hat{P}_l = P_l/(2l+1)$, since there are $2l+1$ modes (orders) per degree—we do not explore this definition of power in this contribution, and present only total power per degree (see, e.g., Hoggard et al., 2016; Holdt et al., 2022).

References

Baumgardner, J. R.: Three-dimensional treatment of convective flow in the Earth's mantle, Journal of Statistical Physics, 39, 501–511, https://doi.org/10.1007/BF01008348, 1985.

Bunge, H.-P. and Baumgardner, J. R.: Mantle convection modeling on parallel virtual machines, Computers in Physics, 9, 207–215, https://doi.org/10.1063/1.168525, 1995.

Davies, D. R., Davies, J. H., Bollada, P. C., Hassan, O., Morgan, K., and Nithiarasu, P.: A hierarchical mesh refinement technique for global 3-D spherical mantle convection modelling, Geoscientific Model Development, 6, 1095–1107, https://doi.org/10.5194/gmd-6-1095-2013, 2013.

Forte, A. M.: Constraints on Seismic Models from Other Disciplines - Implications for Mantle Dynamics and Composition, in: Seismology and the Structure of the Earth, edited by Romanowicz, B. and Dziewonski, A., chap. 1.23, pp. 805–858, Elsevier B.V., ISBN 9780444527486, https://doi.org/10.1016/B978-044452748-6.00027-4, 2007.

Ghelichkhan, S., Bunge, H.-P., and Oeser, J.: Global mantle flow retrodictions for the early Cenozoic using an adjoint method: Evolving dynamic topographies, deep mantle structures, flow trajectories and sublithospheric stresses, Geophysical Journal International, 226, 1432–1460, https://doi.org/10.1093/gji/ggab108, 2021.

Hager, B. H. and O'Connell, R. J.: A Simple Global Model of Plate Dynamics and Mantle Convection, Journal of Geophysical Research, 86, 4843–4867, https://doi.org/10.1029/JB086iB06p04843, 1981.

Hoggard, M. J., White, N., and Al-Attar, D.: Global dynamic topography observations reveal limited influence of large-scale mantle flow, Nature Geoscience, 9, 1–8, https://doi.org/10.1038/ngeo2709, 2016.

Holdt, M. C., White, N. J., Stephenson, S. N., and Conway-Jones, B. W.: Densely Sampled Global Dynamic Topographic Observations and Their Significance, Journal of Geophysical Research: Solid Earth, 127, 1–32, 2022.

McKenzie, D. P., Roberts, J. M., and Weiss, N. O.: Convection in the earth's mantle: Towards a numerical simulation, Journal of Fluid Mechanics, 62, 465–538, https://doi.org/10.1017/S0022112074000784, 1974.

Merdith, A. S., Williams, S. E., Collins, A. S., Tetley, M. G., Mulder, J. A., Blades, M. L., Young, A., Armistead, S. E., Cannon, J., Zahirovic, S., and Müller, R. D.: Extending full-plate tectonic models into deep time: Linking the Neoproterozoic and the Phanerozoic, Earth-Science Reviews, 214, 1–44, https://doi.org/10.1016/j.earscirev.2020.103477, 2021.

Mitrovica, J. X. and Forte, A. M.: A new inference of mantle viscosity based upon joint inversion of convection and glacial isostatic adjustment data, Earth and Planetary Science Letters, 225, 177–189, https://doi.org/10.1016/j.epsl.2004.06.005, 2004.

Panton, J., Davies, J. H., and Myhill, R.: The Stability of Dense Oceanic Crust Near the Core-Mantle Boundary, Journal of Geophysical Research: Solid Earth, 128, 1–21, https://doi.org/10.1029/2022JB025610, 2023.

Parsons, B. and Daly, S.: The relationship between surface topography, gravity anomalies and temperature structure of convection, Journal of Geophysical Research, 88, 1129–1144, https://doi.org/10.1029/JB088iB02p01129, 1983.

Ricard, Y.: Physics of Mantle Convection, in: Treatise on Geophysics, edited by Schubert, G., chap. 7.02, pp. 23–71, https://doi.org/10.1016/B978-044452748-6.00115-2, 2015.

van Heck, H. J., Davies, J. H., Elliott, T., and Porcelli, D.: Global-scale modelling of melting and isotopic evolution of Earth's mantle: Melting modules for TERRA, Geoscientific Model Development, 9, 1399–1411, https://doi.org/10.5194/gmd-9-1399-2016, 2016.
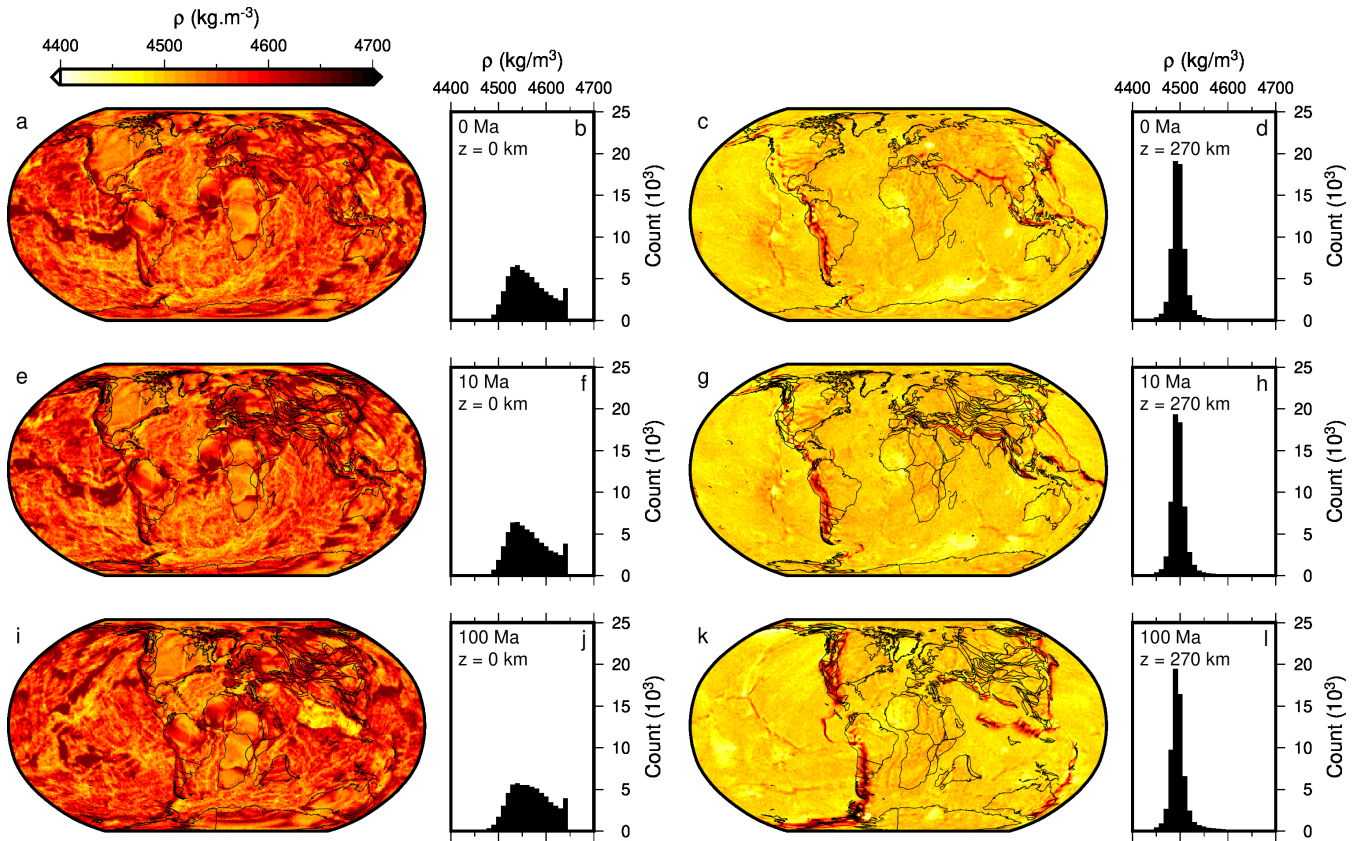
Figure S1. Model 1: Densities predicted from numerical simulation of mantle convection. (a) Predicted present-day density ρ, at surface (z=0), from TERRA model with viscosity independent of temperature (Model 1a), plotted at grid resolution of 1 degree. (b) Histogram of values shown in (a), weighted by latitude to correct to equal-area. (c–d) As (a–b) but for densities at a depth of 270 km. (e–h) As (a–d) but for time slice at 10 Ma; paleo-coastlines generated from Phanerozoic plate rotation history of Merdith et al. (2021). (i–l) As (a–d) but for time slice at 100 Ma.
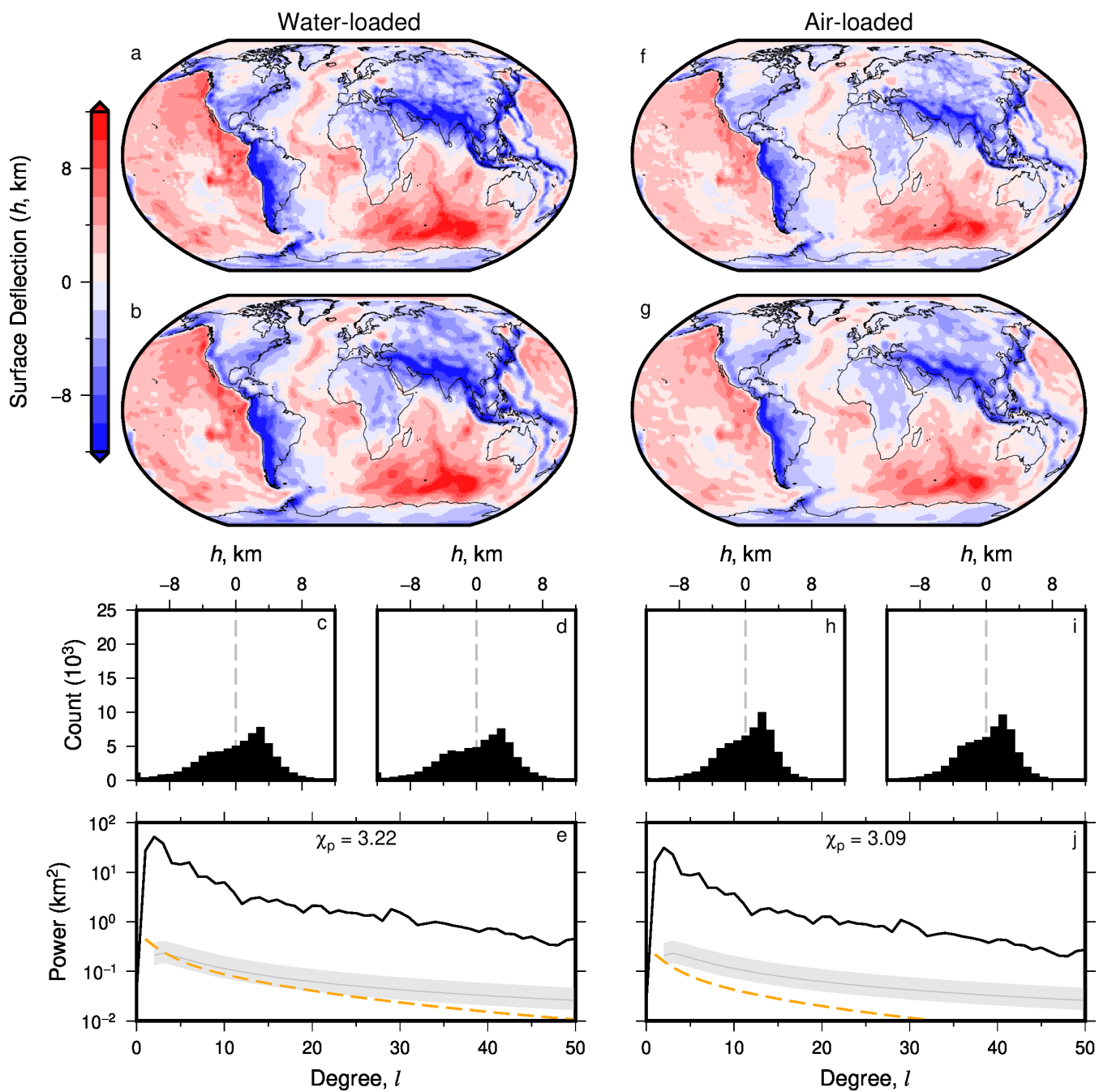
Figure S2. Model 1: Predicted water- and air-loaded surface deflections. (a) Water-loaded, present day, surface deflection predicted by Model 1a. Figure S2a shows normal stress, σ, used with Equation 2 in the main manuscript to calculate surface deflections, h; $\rho_w = 1030$ kg m^{-3}. (b) Spherical harmonic fit (Model 1b) up to degree $l = 50$ of grid shown in (a), calculated using the approach of Hoggard et al. (2016). (c–d) Histogram of values shown in (a) and (b) respectively, weighted by latitude to correct to equal-area. (e) Black line = power spectrum in terms of total power per degree, from spherical harmonic expansion shown in (b); gray line and band = expected dynamic topography from Kaula's rule using admittance $Z = 12 \pm 3$ mGal km^{-1} (Kaula, 1963). Orange dashed line = expected power spectrum for water-loaded residual topography from Holdt et al. (2022) via analytical solution of special case of Equation 4 of the main manuscript. χ_p = total root-mean-squared difference between distribution of modeled and theoretical surface deflection power (see Equation 9 in the main manuscript). (f–j) As (a–e) but for air-loaded surface deflection; $\rho_w = 1$ kg m^{-3}.
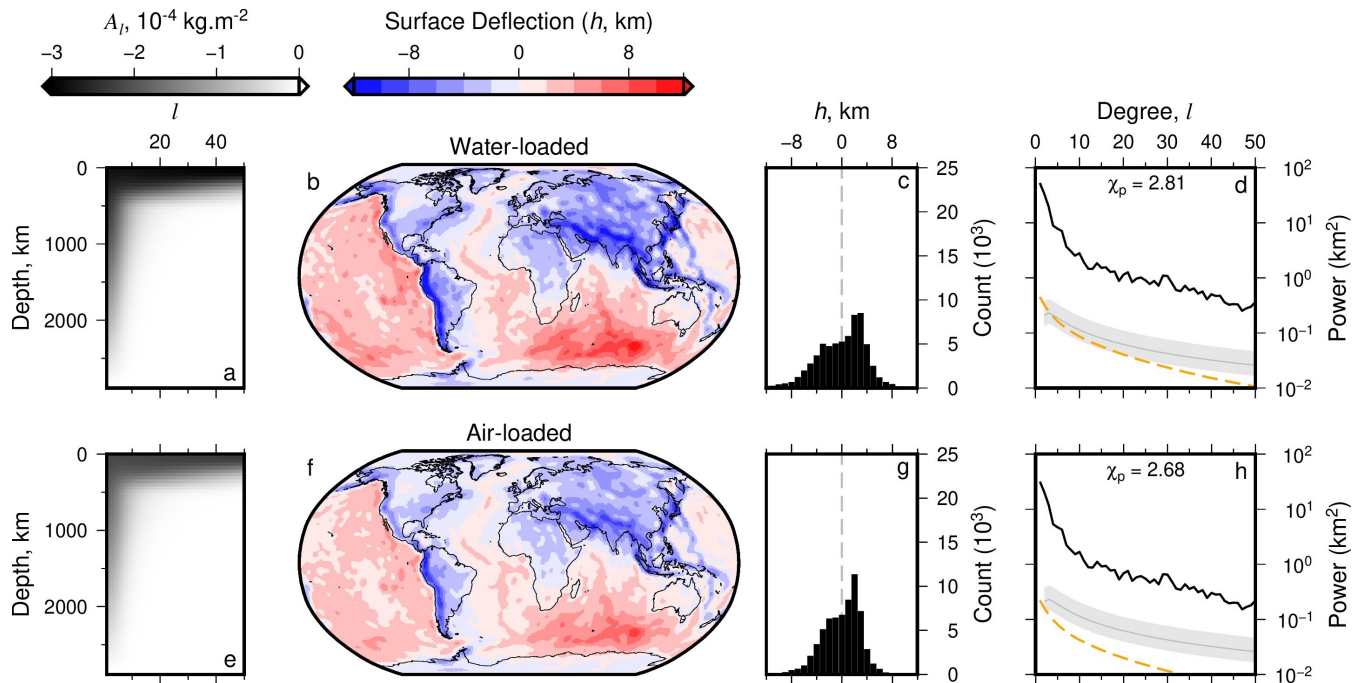
Figure S3. Model 2: Propagator matrix solution for surface deflection with associated sensitivity kernels. (a) Surface deflection sensitivity kernel A_l, as a function of spherical harmonic degree, l, and depth, calculated for the radial viscosity structure (and other parameters) which were used to generate Model 1; see Equation 5 in the main manuscript. (b) Present-day predicted water-loaded surface deflection, calculated using propagator matrix method, from spherical harmonic expansion (to maximum degree $l = 50$) of density structure (e.g., Figure S1) and radial viscosity structure (e.g., Figure 2c; Corrieu et al., 1995; Hager et al., 1985; Parsons & Daly, 1983). Note that for comparison with numeric calculations shown in Figure 3, no terms related to flow-related perturbation of gravitational potential terms are included (see Equations 5 and 6 in the main manuscript), and gravitational acceleration $g = 10$ m s^{-2} everywhere. (c) Histogram of values shown in (b), weighted by latitude to correct to equal-area. (d) Black line = power spectrum in terms of total power per degree, from surface deflection prediction shown in (a); gray line and band = expected dynamic topography from Kaula's rule using admittance $Z = 12 \pm 3$ mGal km^{-1} (Kaula, 1963). Orange dashed line = power spectrum of water-loaded residual topography from Holdt et al. (2022), via analytical solution of special case of Equation 4 in the main manuscript. χ_p = total root-mean-squared difference between distribution of modeled and theoretical surface deflection power (see Equation 9 in the main manuscript). (e–h) As (a–d) but for air-loaded surface deflection; $\rho_w = 1$ kg m^{-3}.
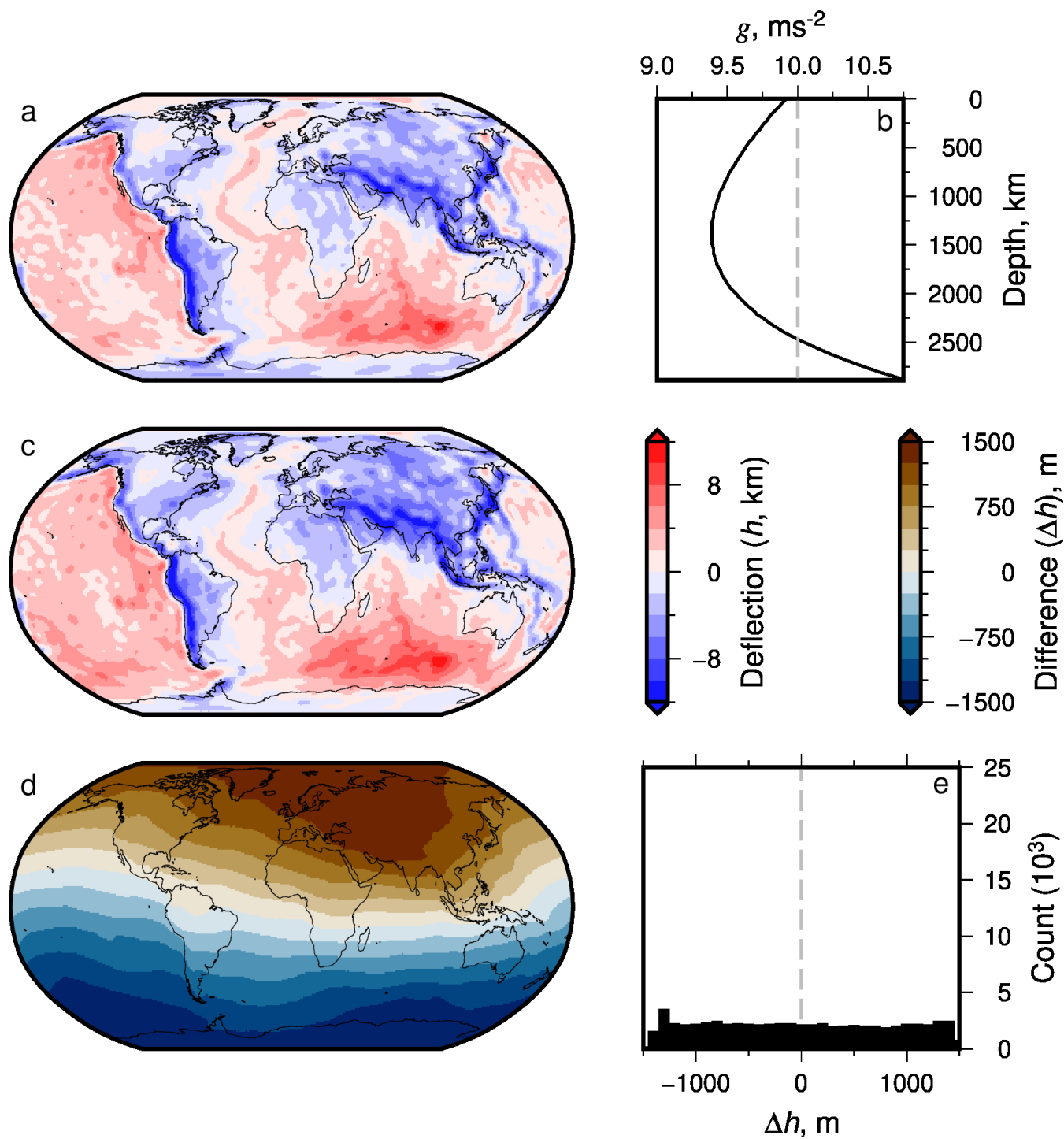
Figure S4. Model 3: Predicted surface deflection from mantle convection in presence of radial gravitation. (a) Predicted present-day water-loaded surface deflection calculated using propagator matrix method, incorporating radial gravitation i.e., $g(r)$, black curve in (b).(b) Black curve = profile of gravitational acceleration as a function of radius, given density distribution predicted by Model 1a; gray dashed line = constant value of $g = 10$ m s^{-2} used within TERRA model runs and in previous figures. (c) As (a) but calculated using $g = 10$ m s^{-2} everywhere, i.e., same as Figure S3a–d (see dashed line in panel b). Associated sensitivity kernels are shown in Figure S6. (d) Difference between surface deflections predicted by Models 3 and 2 (panels a and c). (e) Histogram of values in (d), weighted by latitude to correct to equal-area.
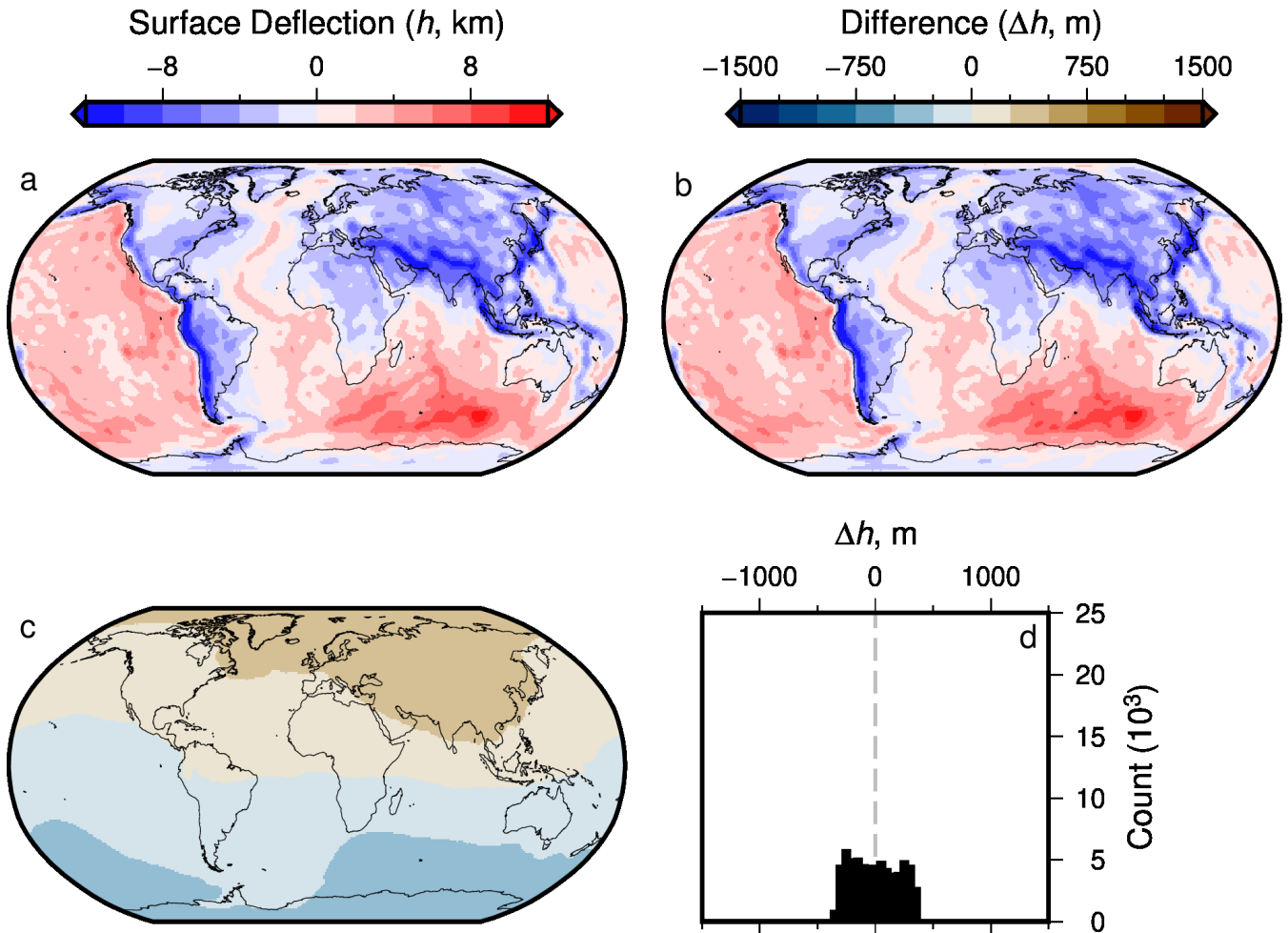
Figure S5. Model 4: Comparing predicted surface deflections with and without stress perturbations induced by gravitational potential of deflected surface. (a) Predicted present-day water-loaded surface deflection calculated using propagator matrix method, with $g = 10$ m s^{-2} everywhere, including terms describing stress perturbation due to change in gravitational potential (i.e., u_3 term in Equation 5 in the main manuscript). (b) As (a) but calculated excluding u_3 term, i.e., same as Figure S3a. See Figure S6 for associated sensitivity kernels. (c) Difference between Models 4 and 2 (panels a and b). Note same colour scales are used as in Figure S4. (d) Histogram of values in (d), weighted by latitude to correct to equal-area.
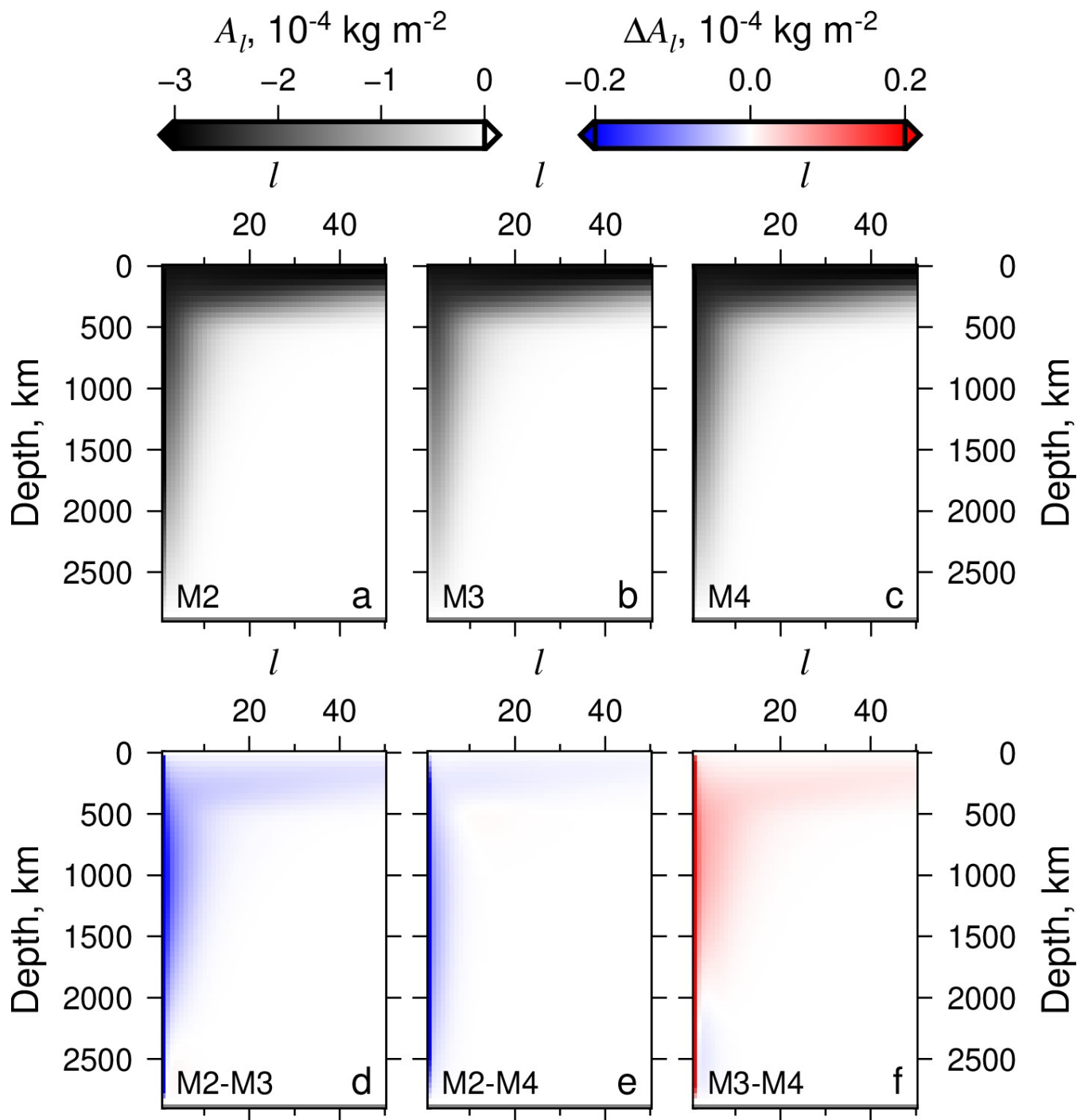
Figure S6. Comparison of sensitivity kernels generated with different treatment of gravitation. (a–c) Sensitivity kernels of Models 2 (M2; $g = 10$ m s^{-2}), 3 (M3; $g = g(r)$) and 4 (M4; gravitational potential of perturbed surface is included and $g = 10$ m s^{-2}); see Figures 3–4 & S3–S5. (d) Comparison of sensitivity kernels from Models 2 and 3; Model 3 kernel is subtracted from Model 2 kernel. (e–f) Comparisons of kernels from Models 2 & 4, and 3 & 4.
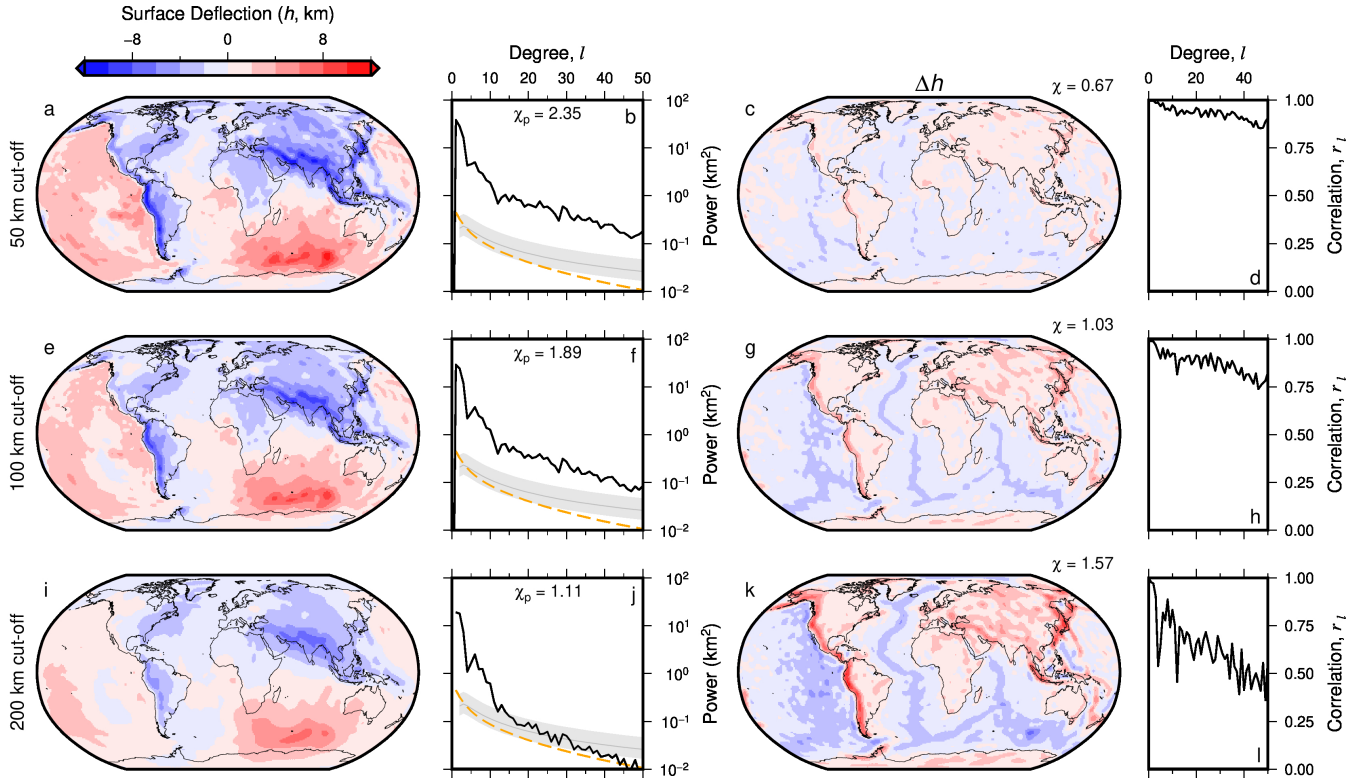
Figure S7. Models 5–7: Effect of removing shallow structure from analytic surface deflection calculations. (a) Model 5: Predicted water-loaded surface deflection from propagator matrix solution for Model 2, i.e., as Figure S3b, but with effect of upper 50 km of density anomaly structure ignored in calculation. (b) Black line = power spectrum of surface deflection shown in (a); gray line and band = expected dynamic topography from Kaula's rule using admittance $Z = 12 \pm 3$ mGal km^{-1} (Kaula, 1963). Orange dashed line = expected power spectrum for water-loaded residual topography from Holdt et al. (2022), via analytical solution of special case of Equation 4 in the main manuscript. $\chi_p =$ total root-mean-squared difference between distribution of modeled and theoretical surface deflection power (see Equation 9 in the main manuscript). (c) Difference between Models 5 and 2, i.e., between panel (a) and original propagator matrix solution, Model 2, shown in Figure S3b. (d) Spectral correlation coefficient, r_l, between Model 5 and 2; Equation 8 in the main manuscript. (e–h) and (i–l) as (a–d) but for depth cut-offs of 100 (Model 6) and 200 km (Model 7), respectively.
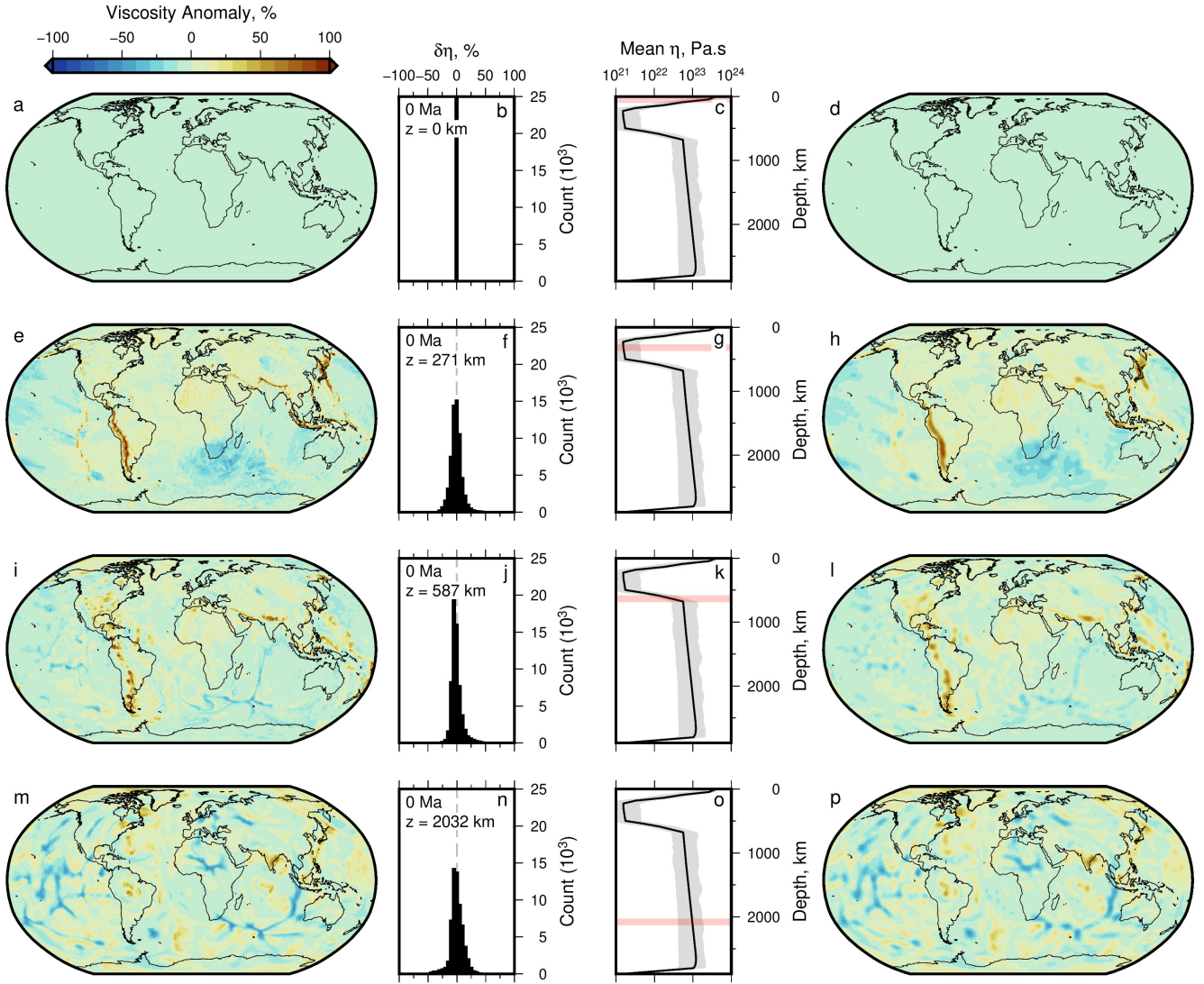
Figure S8. Model 11: Numerical simulation of mantle convection with temperature dependent viscosity, η, and spherical harmonic representation. (a) Present-day viscosity at surface from Model 11a, expressed as percentage deviation from layer mean, $\delta\eta$, plotted at grid resolution of 1 degree. (b) Histogram of values shown in (a), weighted by latitude to correct to equal-area. (c) Black line and gray band = global mean and extreme viscosity values as a function of depth; pink band = depth slice shown in (a). (d) Model 11b: Spherical harmonic fit up to degree $l = 50$ of grid shown in (a), using inverse approach of Hoggard et al. (2016). (e–h) As (a–d) but for depth slice at 271 km below surface. (i–l) and (m–p) 587 km and 2032 km depth slices.
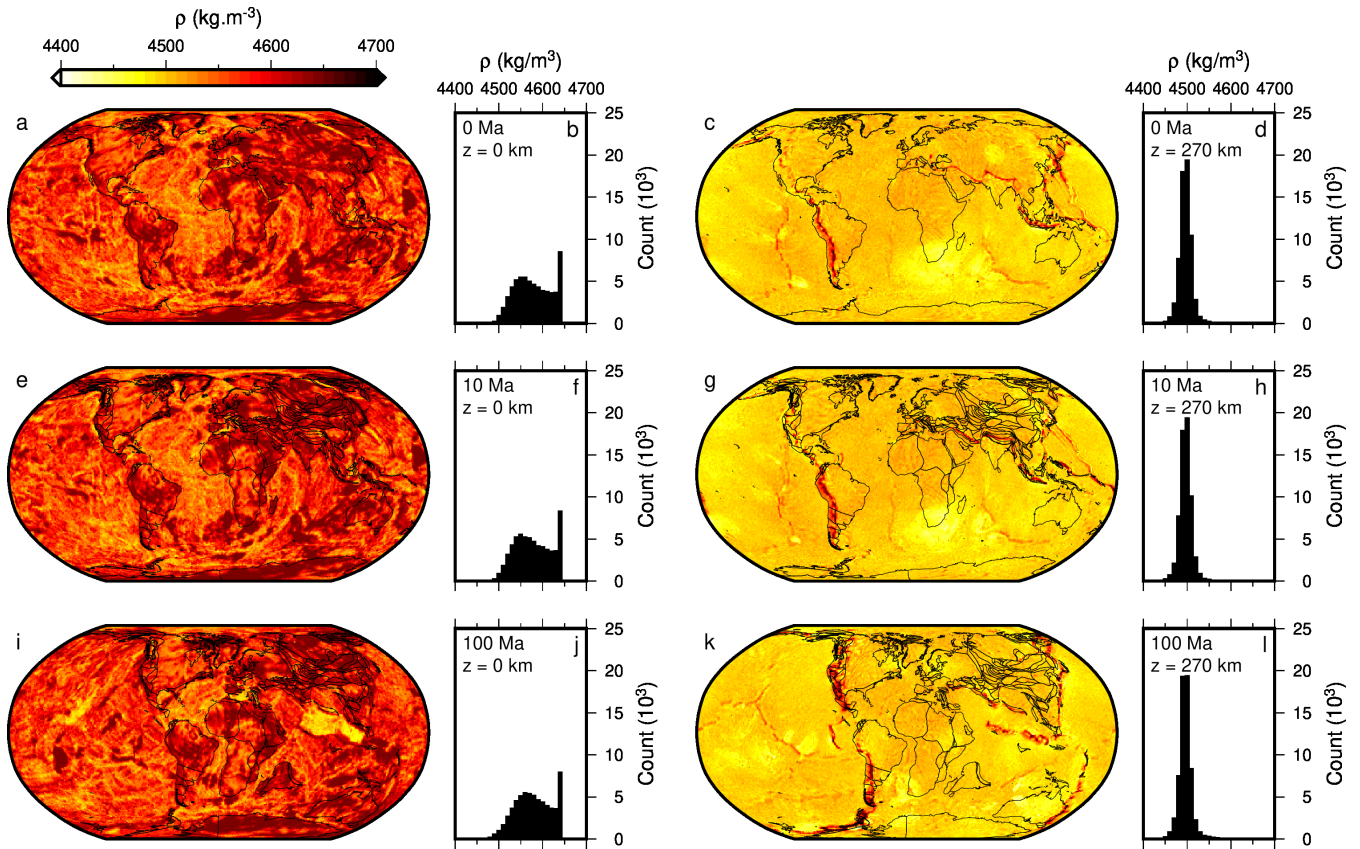
Figure S9. Model 11: Densities predicted by numerical simulation with temperature-dependent viscosity. (a) Predicted present-day density ρ, at surface (z=0), from TERRA model. (b) Histogram of values shown in (a), weighted by latitude. (c–d) As panels (a–b) but for densities at 270 km depth. (e–h) and (i–l) As panels (a–d) for time slices at 10 and 100 Ma (see caption of Figure S1 for expanded description; Figure S8 for viscosity structure; Equation S7 of this document).
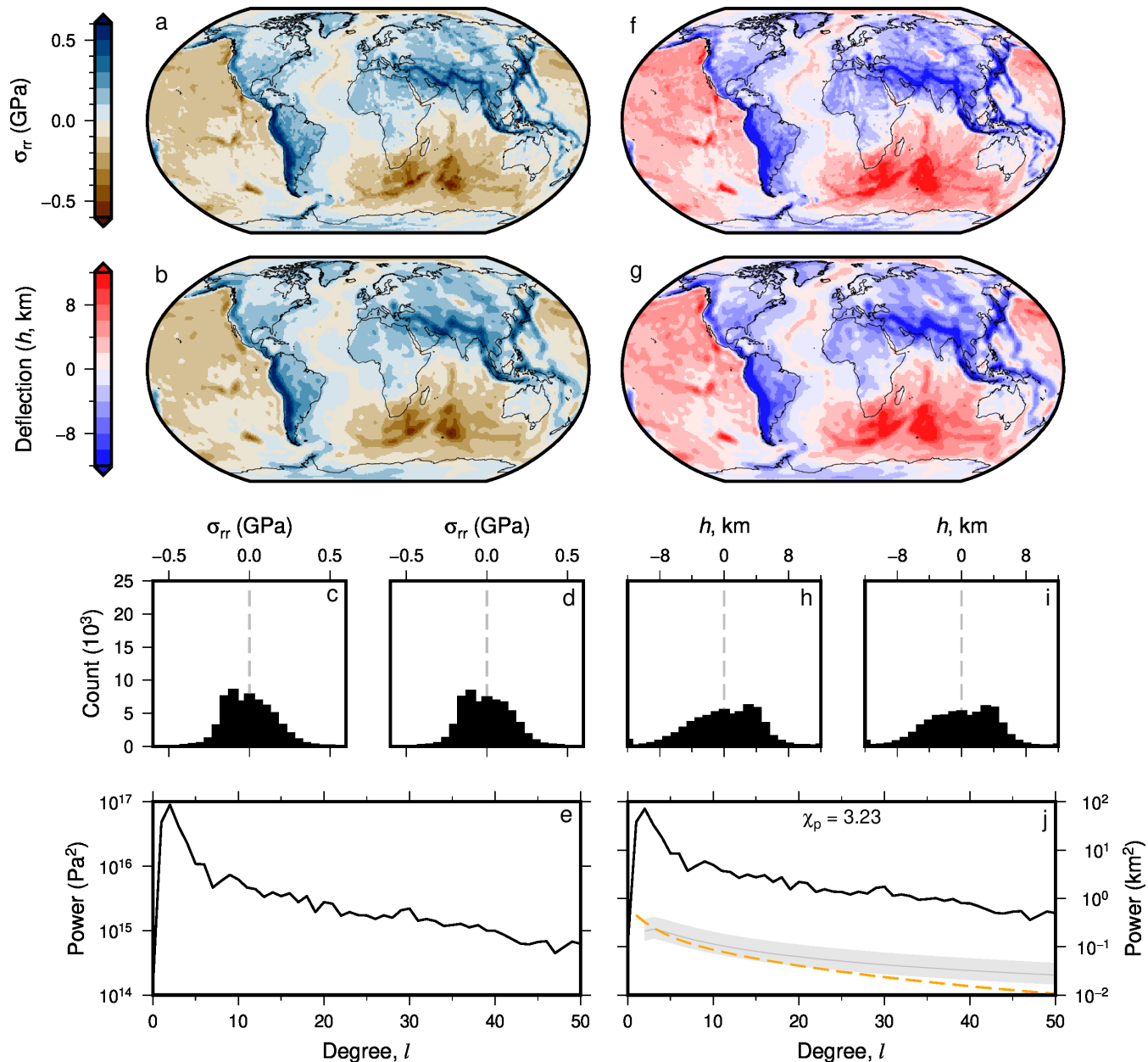
Figure S10. Model 11: Predictions of surface stresses and deflections from simulations with temperature dependent viscosity. (a) Predicted present-day surface radial stress, σ_{rr} from numerical TERRA model (Model 11a), plotted at grid resolution of 1 degree. (b) Model 11b: Spherical harmonic representation of Model 11a up to degree $l = 50$. (c) Histogram of values shown in (a), weighted by latitude to correct to equal-area. (d) Histogram of values shown in panel (b). (e) Power spectrum of surface stresses. (f–i) Calculated water-loaded surface deflections and associated histograms for full resolution numerical solutions (f, h) and spherical harmonic representation (g, i). (j) Power spectrum (black) of water-loaded surface deflection (panel g), Kaula's rule (grey curve and band), and water-loaded residual topography (orange); see Figure S2 for expanded description.
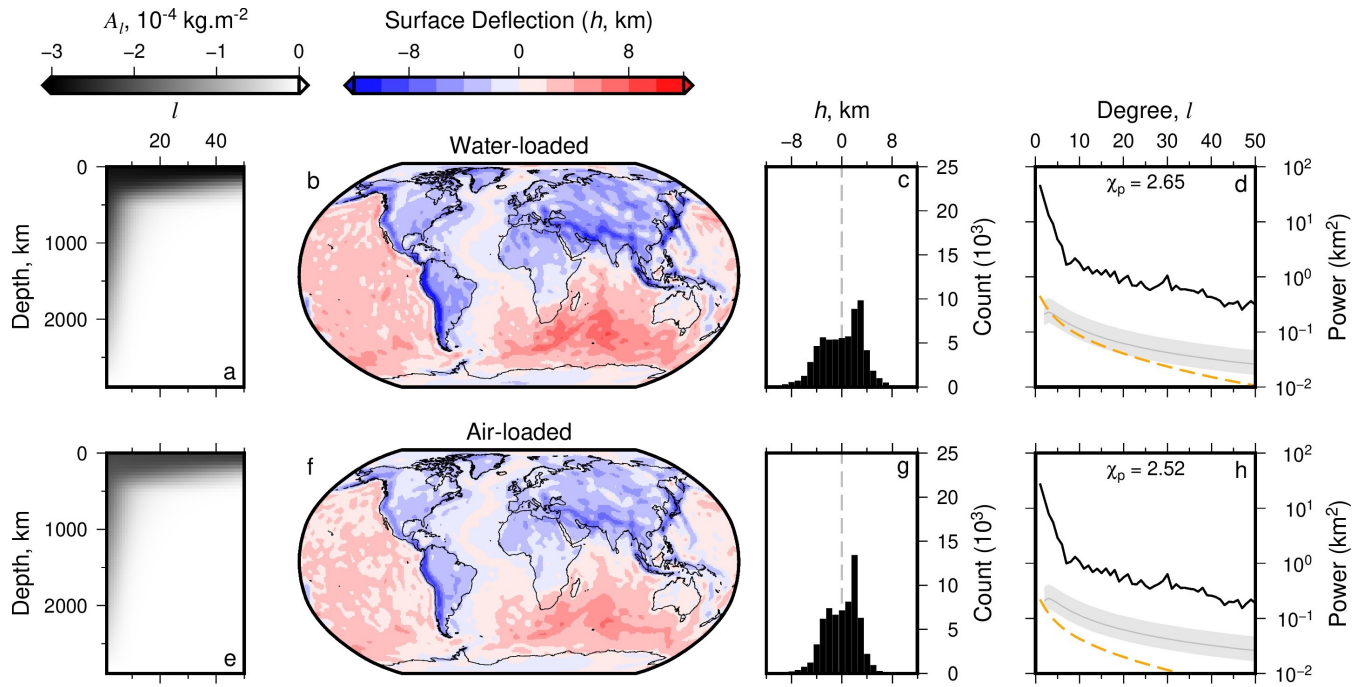
Figure S11. Model 12: Analytical (propagator matrix) predictions of surface deflections from simulations with temperature dependent viscosity. Radial viscosity is calculated using mean (radial) values from numerical model with temperature-dependent viscosity (i.e., Model 11a; Figure S10). (a–d) Present-day, water-loaded, surface deflection calculated analytically using propagator matrix solution; see Figure S3 for expanded description of panels. (e–h) Air-loaded deflection and associated metrics.
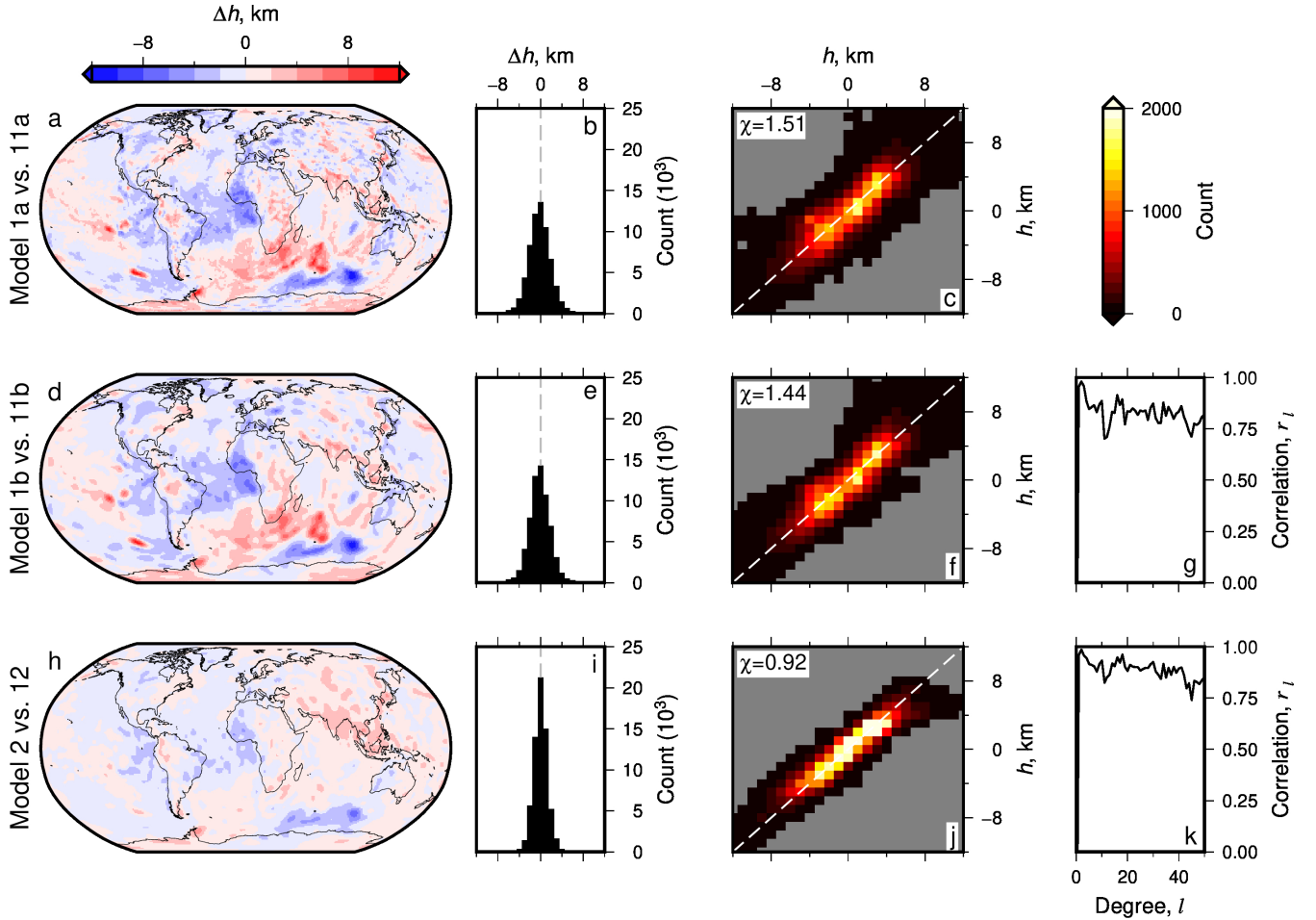
Figure S12. Comparing surface deflections calculated using normal stresses from numeric simulations (Models 1 and 11) and analytic estimates (Models 2 and 12) with and without temperature dependent viscosity. (a) Difference in predicted surface deflection, Δh, between numerical simulations with (Model 11a) and without (Model 1a) temperature-dependent viscosity. Full-resolution surface radial stresses are converted into surface deflections, h, using Equation 2 of the main manuscript. (b) Histogram of values shown in (a). (c) Pixel-wise comparison of predicted surface deflection between the two models; χ = root-mean-squared difference between predictions, see Equation 7 of the main manuscript; gray dashed line = 1:1 ratio. (d–f) as (a–c) but for surface deflection calculated using spherical harmonic expansion of surface radial stresses (Model 1b vs. 11b). (g) Spectral correlation coefficient, r_l, between model predictions (with and without temperature dependent viscosity; see Equation 8 of the main manuscript). (h–k) as (d–g) but for surface deflections calculated for each model using the propagator matrix approach (Model 2 vs. 12).
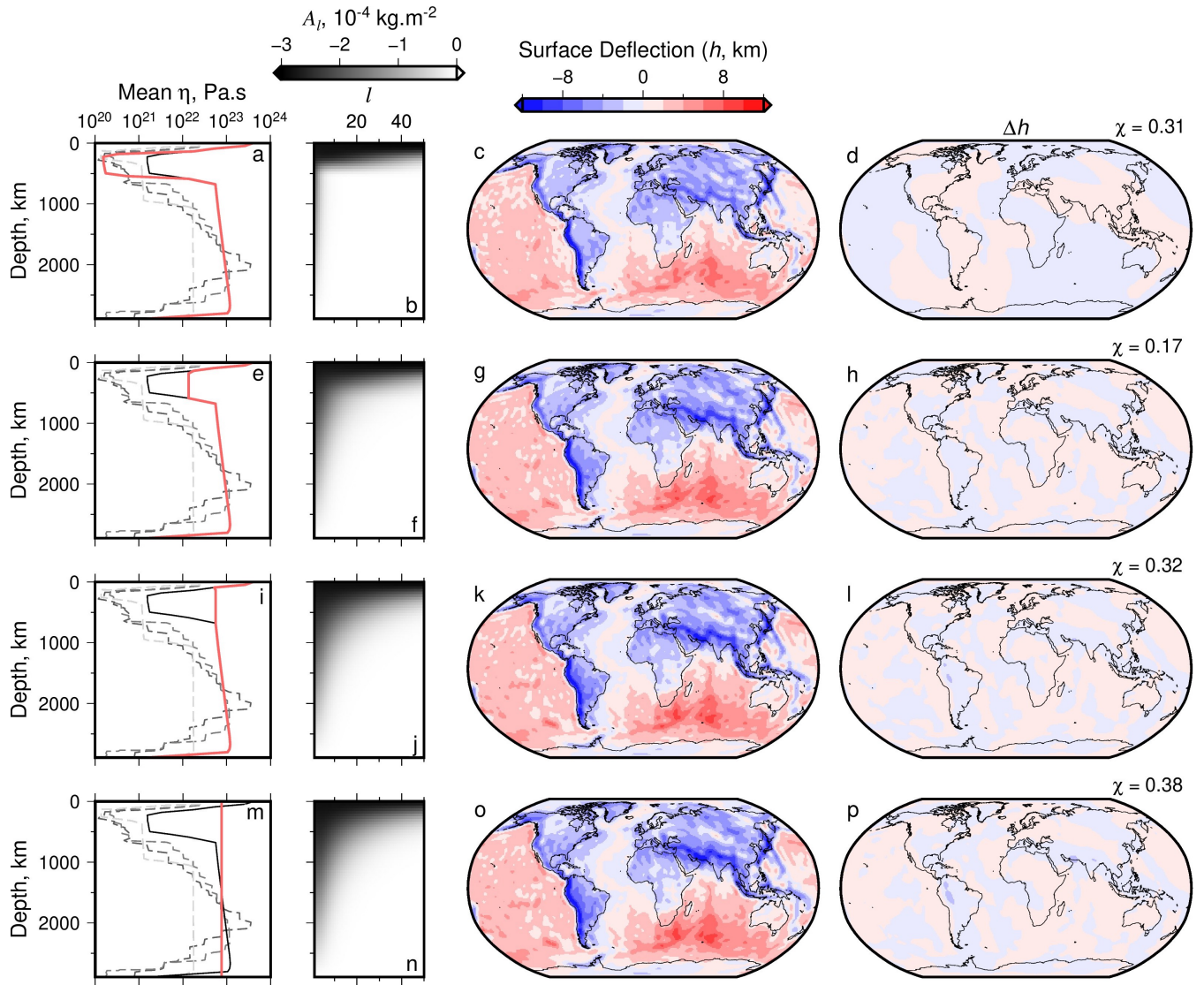
Figure S13. Models 13–16: Sensitivity of calculated analytic surface deflection to adjusted radial viscosity. (a) Model 13: Black curve = prediction of present-day radial mean viscosity from Model 11; red line = adjusted radial profile with viscosity decreased by a factor of 10 between depths of $\sim$ 300–500 km; gray dashed lines = viscosity profiles used in other studies (see Figure 2c). (b) Sensitivity kernel generated using adjusted viscosity shown in (a). (c) Surface deflection calculated using propagator matrix approach parameterised using adjusted viscosity profile (red curve in panel a), and resulting sensitivity kernel shown in panel (b). (d) Difference between propagator matrix solutions generated using adjusted and un-adjusted viscosity profiles, i.e., panel (c) minus Figure 7b (Model 13 vs. 12). Value of root-mean-squared difference, χ, (between calculated surface deflections for un-adjusted and adjusted viscosity) is stated (see Equation 7 of the main manuscript). (e–h) Model 14: As (a–d) but applying an increase in viscosity of a factor of 10 between $\sim$ 300–500 km. (i–l) Model 15: As (a–d) but applying an increase in viscosity of a factor of 100 between $\sim$ 300–500 km. (m–p) Model 16: As (a–d) but applying an constant viscosity of $\approx 7.5 \times 10^{22}$ Pa s (i.e., the mean value of the reference profile) across all depths.
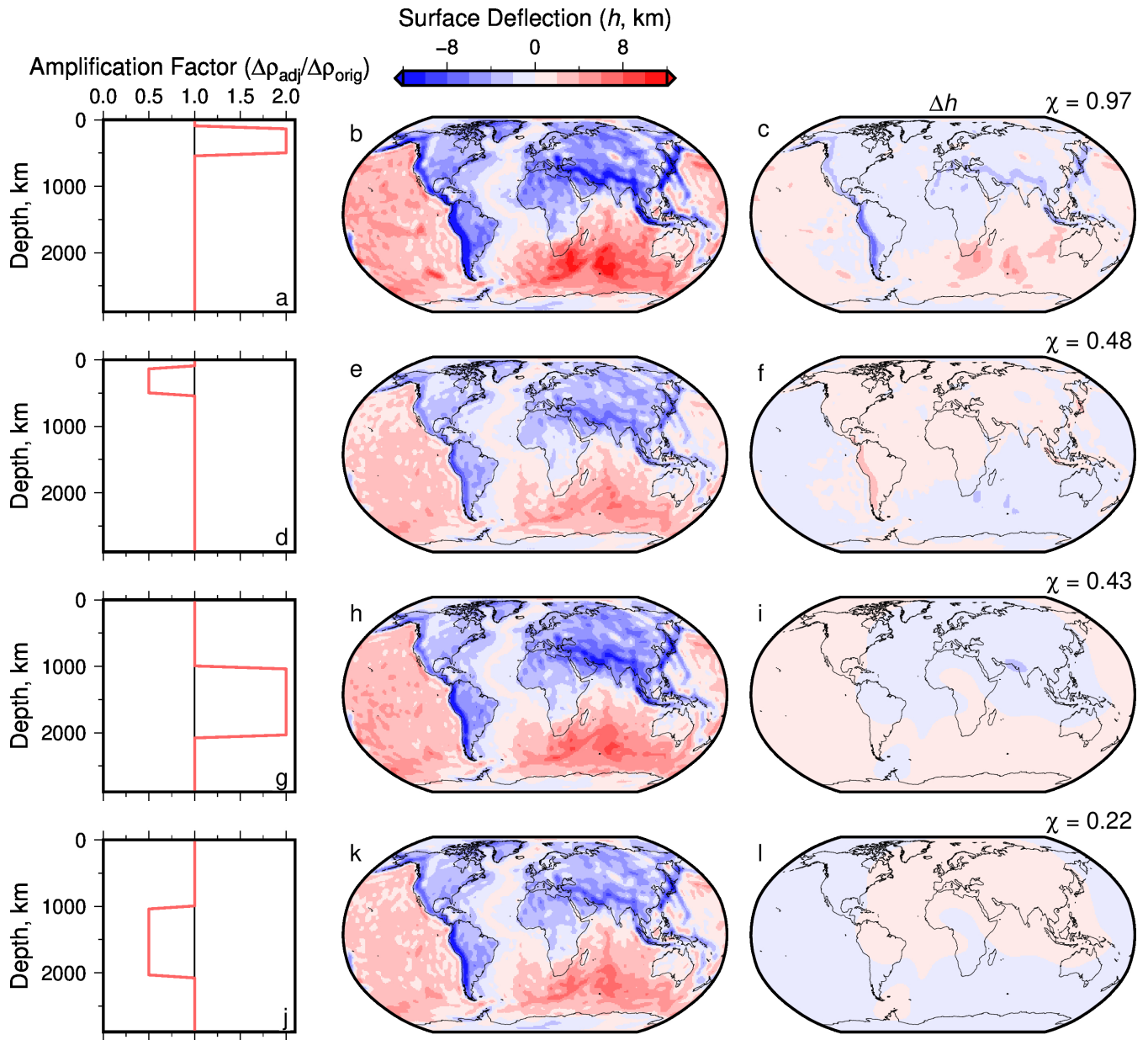
Figure S14. Models 17–20: Sensitivity of calculated analytic surface deflection to adjusted density anomalies. Annotation is as for Figure S13 but for adjusted density anomalies (red lines in left panels), by directly scaling spherical harmonic coefficients ($l > 0$) up or down by a factor of 2 (Models 17 & 19, panels a–c & g–i, respectively) or $\frac{1}{2}$ (Models 18 & 20: d–f & j–l). Viscosity structure applied in each case is same as that used to generate Figure 7b. Sensitivity kernels for surface deflection are not shown since they are invariant with respect to density anomalies, $\Delta\rho$, depending only on viscosity structure.
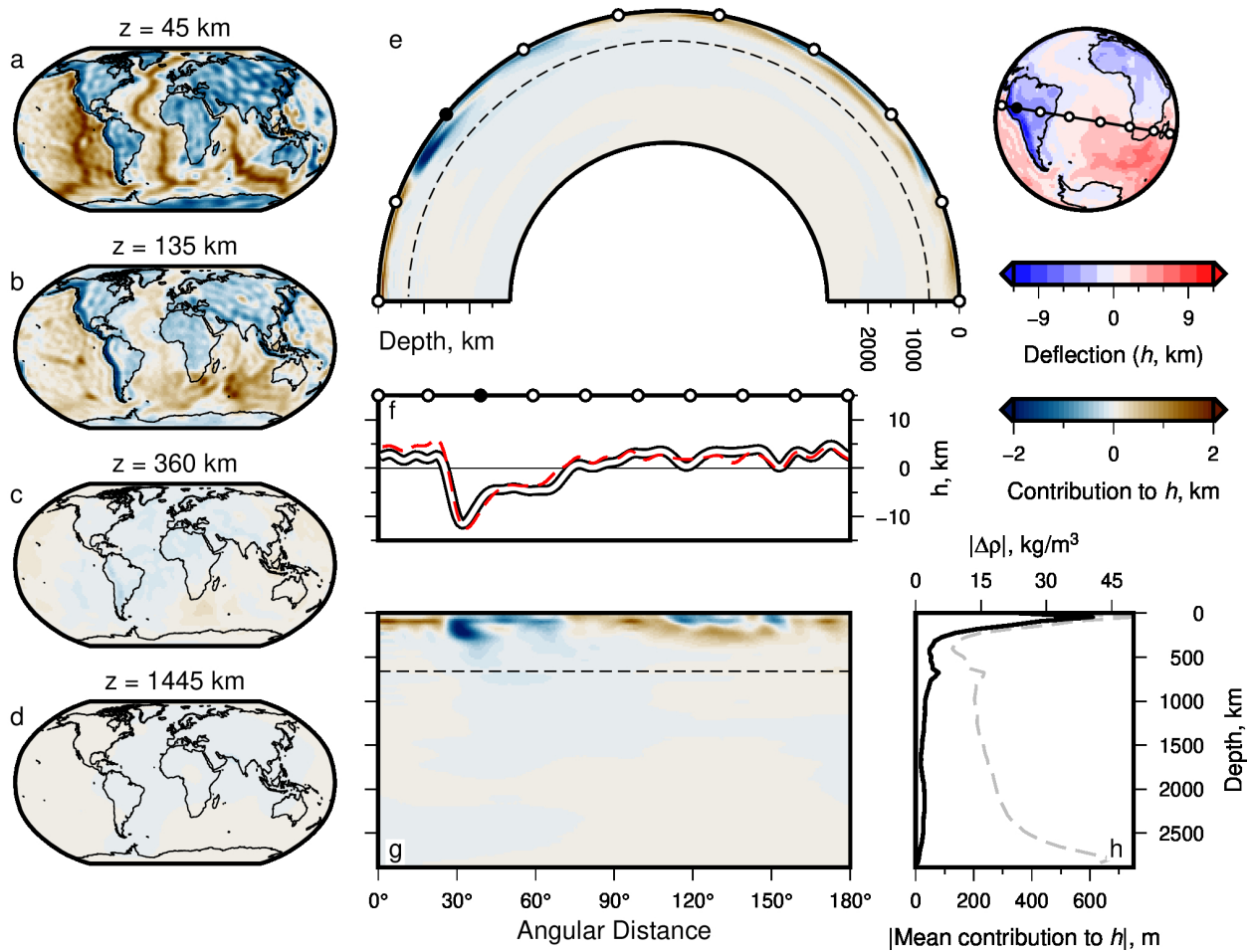
Figure S15. Surface deflections and effective densities up to maximum degree 40. (a–d) Net contribution to present-day water-loaded surface deflection calculated using analytical approach with maximum $l = 40$. Depth slices at 45, 135, 360 and 1445 km depth. (e) Great-circle slice (180°) showing contributions to surface deflection; globe to right shows transect location and calculated surface deflection, up to maximum $l = 40$. White circles = 20° intervals; filled black circle is for orientation; dashed line = 660 km depth contour. (f) White-black curve = surface deflection along transect shown atop globe in panel (e); red dashed curve = surface deflection from Model 2. (g) Cartesian version of panel (e). (h) Grey dashed curve = mean absolute value of density anomalies in Model 12—see top axis for values. Black curve = global mean amplitude (modulus) of contribution from density structure up to maximum $l = 40$ to total surface deflection h.
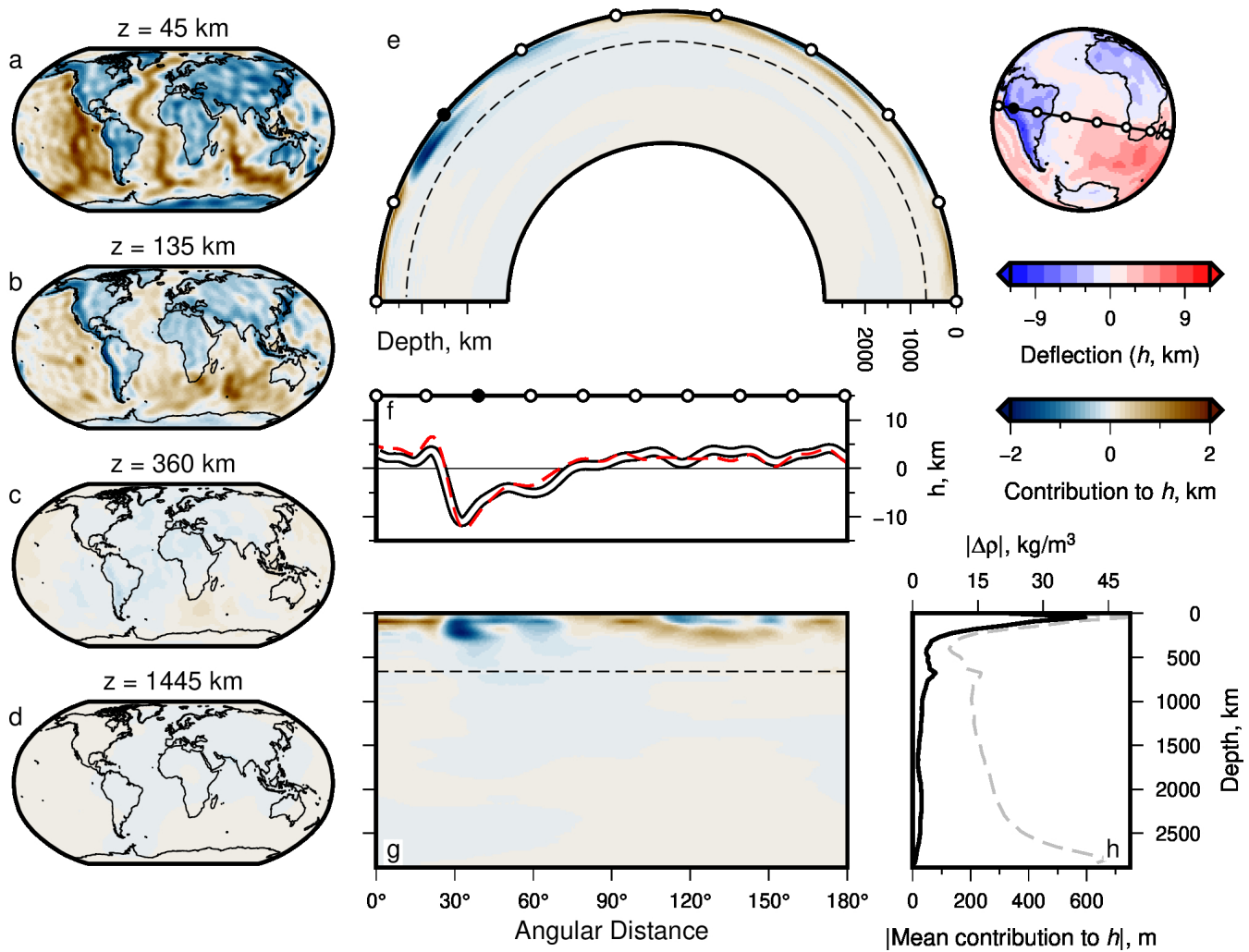
Figure S16. Surface deflections and effective densities up to maximum degree 30. As Figure S15, but for maximum spherical harmonic degree $l = 30$.
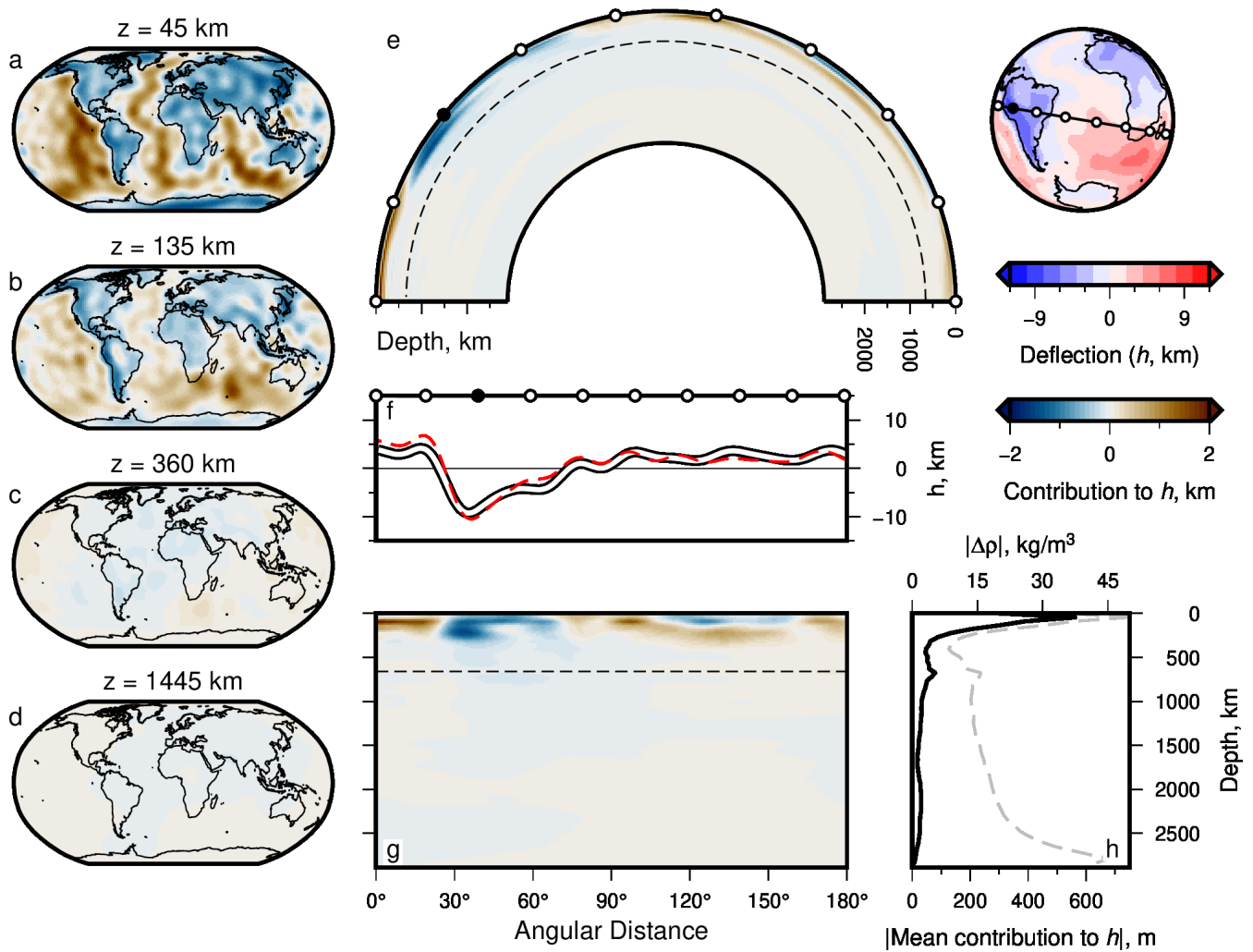
Figure S17. Surface deflections and effective densities up to maximum degree 20. As Figure S15, but for maximum spherical harmonic degree $l = 20$.
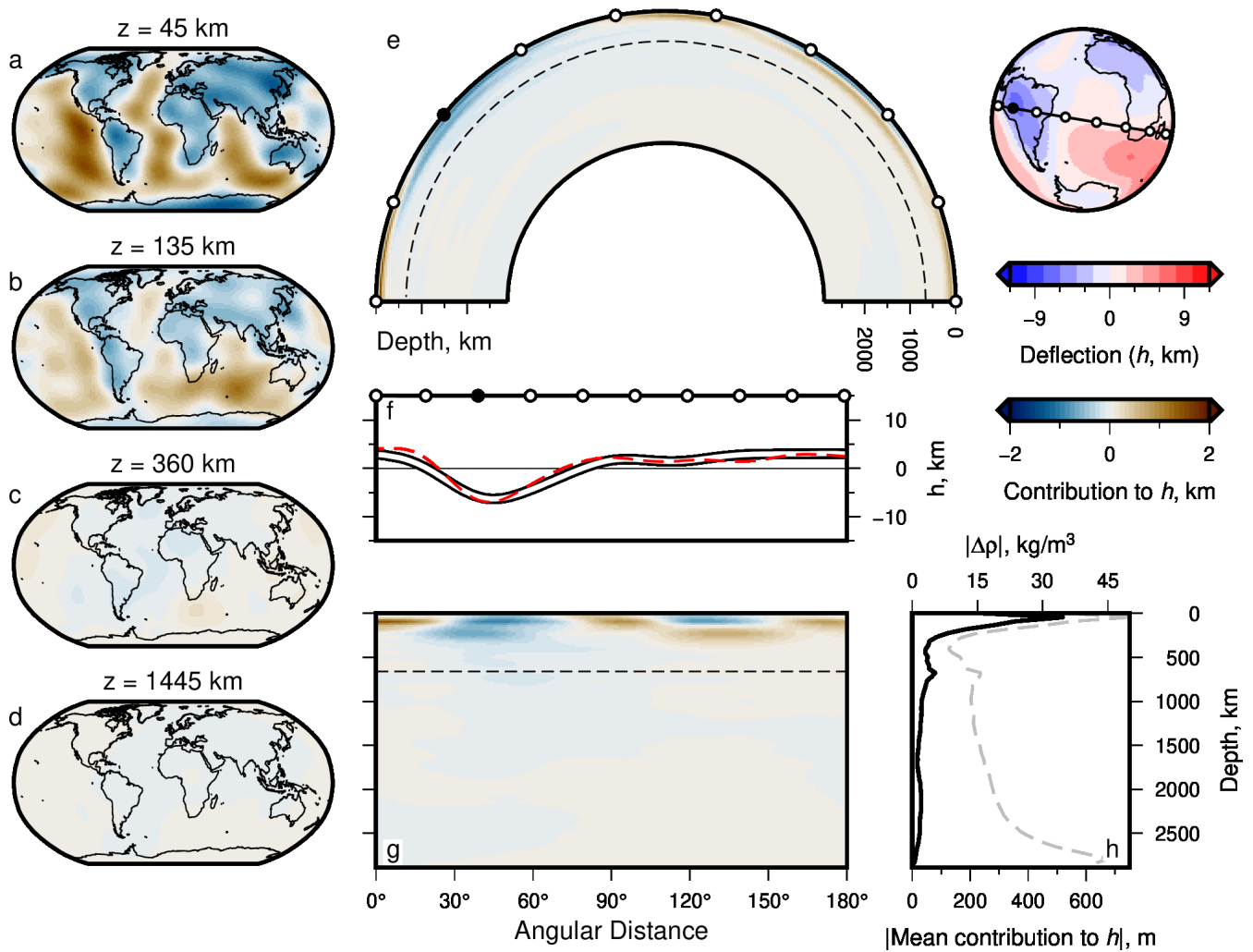
Figure S18. Surface deflections and effective densities up to maximum degree 10. As Figure S15, but for maximum spherical harmonic degree $l = 10$.
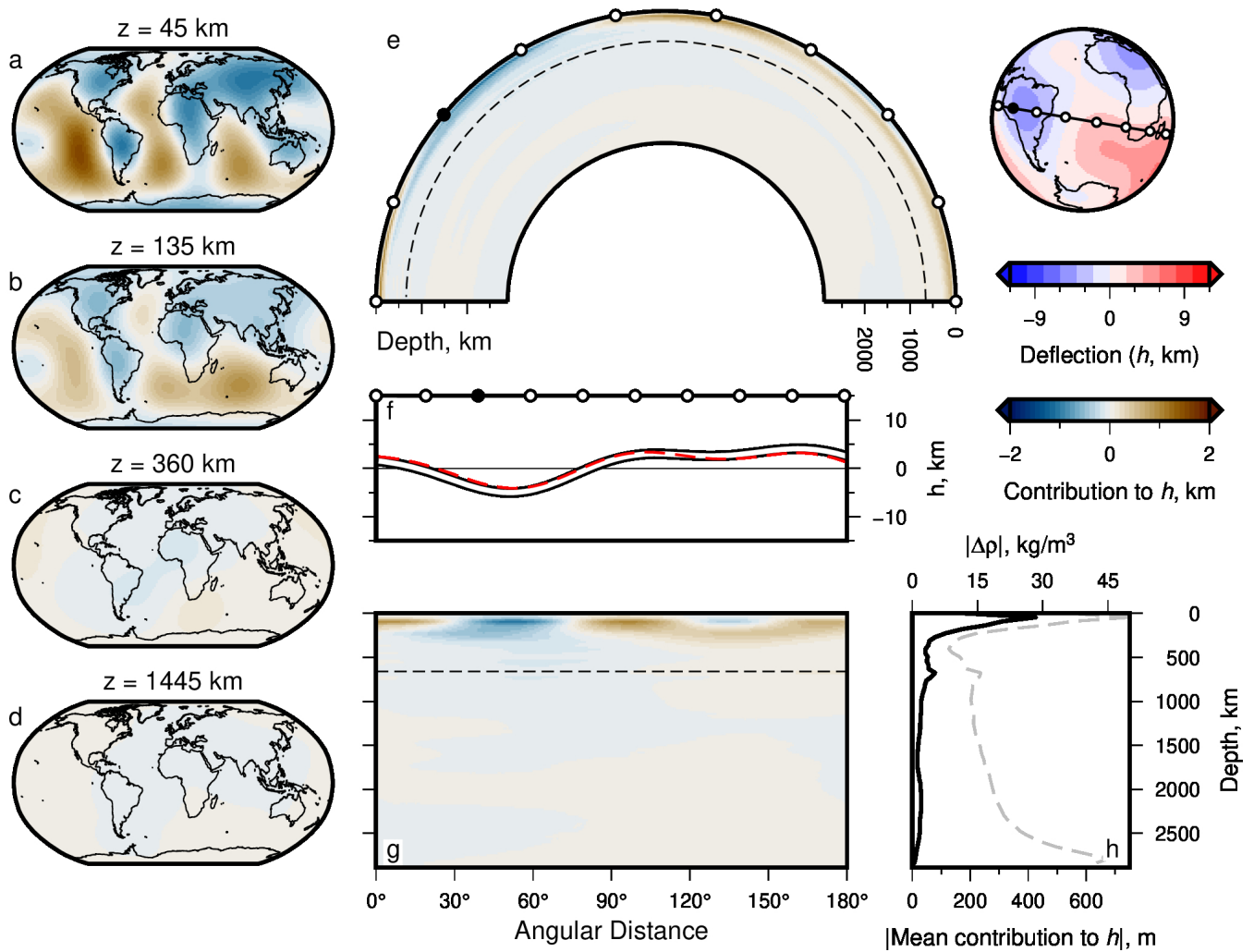
Figure S19. Surface deflections and effective densities up to maximum degree 5. As Figure S15, but for maximum spherical harmonic degree $l = 5$.